

Artificial Neural Network as a Tool to Compensate for Scatter and Attenuation in Radionuclide Imaging

Philippe Maksud, Bernard Fertil, Charles Rica, Georges El Fakhri and André Aurengo
Institut National de la Santé et de la Recherche Médicale Unité 66, Paris, France

This study investigates the ability of artificial neural networks (ANN) to simultaneously correct for attenuation and Compton scattering in scintigraphic imaging. **Methods:** Three sets of experiments are conducted using images of radioactive sources with various shapes and distributions in a homogeneous medium. Numerical Monte Carlo simulations and physical phantom acquisitions of radioactive geometric sources provide the basic material for correction. Our method is based on the following assumptions: information needed to correct for scattering can be extracted from the energy spectrum at each pixel without any assumption concerning the source distribution, and two diametrically opposed energy spectrum acquisitions yield enough information on the source location in the diffusing medium for simultaneous correction for attenuation and scattering. **Results:** Qualitative and quantitative evaluations of scatter correction by ANN demonstrate its ability to perform scatter correction from the energy spectra observed in each pixel. By using the energy spectra of incident photons detected in two diametrically opposed images, multilayer neural networks are able to perform a proper restitution of projection images without any assumption on geometry or position of radioactive sources in simple geometric cases. ANN corrections compare favorably to those provided by five of the most popular methods. A satisfying correction of both scatter and attenuation is observed for a human pelvis scan obtained during routine clinical practice. **Conclusion:** An ANN is an efficient tool for attenuation and Compton scattering in simple model cases. The results obtained for routine scintigrams in a much more complex situation are strong incentives for performing further studies.

Key Words: artificial neural networks; Monte Carlo simulation; Compton scattering correction; attenuation correction

J Nucl Med 1998; 39:735-745

Useful information in conventional nuclear medicine images is impaired by photon attenuation and scattering. These effects are related to the wide energy window settings (20% round the photopeak) that must be used to shorten image acquisition time (this conventional approach will be referred to as F20 thereafter). Contrast is reduced, objects edges are blurred; quantitative analysis is not feasible. Quantitation of regional concentrations of radioisotope from the images, therefore, requires a proper correction.

Many methods have been described to correct for Compton scattering, mainly acquisition of scattered events in a separate energy discrimination window (1), asymmetric photopeak windows (2), dual photopeak windows (3), triple-energy windows (4-6) and image deconvolution by a scatter distribution function (7-10).

Among more recent methods, the spectral approach is promising but requires specialized hardware for energy spectrum acquisition. The unscattered and scattered photon distributions in each pixel are obtained by a polynomial model (11), models derived from Klein and Nishina equations (12), holospectral

imaging (a principal component analysis) (13,14) or factorial analysis of the energy spectrum (15-19). All these methods require additional procedures to handle attenuation. A precise knowledge of the radioactive source distribution is then needed.

Artificial neural networks (ANN) have demonstrated efficiency for generalization, interpolation and extraction of information embedded in complex data. They have been used for image restoration (20,21), lesion detection (22-24) or clinical diagnostic tasks (25-34). An artificial neural network has been used by Ogawa (35) to separate unscattered and scattered photons. By using five small windows along the energy spectrum and a rather simple neural network, an accurate estimation of primary photons was achieved with an error ratio of 5%. Simultaneous correction of attenuation and scatter has also been demonstrated using an ANN for tomographic image reconstruction (SPECT) with impressive efficiency (36). In both situations, the use of ANN results in a significant improvement of quantitative accuracy.

To avoid resorting to a geometric mean or attenuation matrix, we proposed combining these two approaches to address the problem of simultaneous correction for attenuation and scatter when two diametrically opposed views are available. The purpose of this study is to use a neural network method to perform simultaneous correction for scattering and attenuation on limited series of spectral images. Our approach relies on the following assumptions:

1. The information needed to correct scattering can be extracted from the energy spectrum at each pixel without any assumption on the source distribution.
2. Two diametrically opposed energy spectrum acquisitions yield enough information about the source location in the diffusing medium for simultaneous correction of attenuation and scattering.
3. For physical phantoms, acquisitions in air can be considered as scattering and attenuation-free images and, therefore, be used as targets for neural network learning.

In the first part of the study, we investigate the ability of an ANN to correct scattering from the energy spectrum observed at each pixel of the image. In the second part, we evaluate the ability of ANN to correct for attenuation using two diametrically opposed acquisitions of punctual sources. In the third part, the ANN's ability to correct for both scatter and attenuation is assessed. Finally, a clinical case (pelvic bone scan) is used to visually appreciate the quality of correction.

MATERIALS AND METHODS

Numerical Simulations of Radioactive Sources

All sources were simulated in a $20 \times 20 \times 200$ -cm water phantom. Monte Carlo simulations of punctual, linear, planar and volumic (a sphere and a cylinder) radioactive sources at multiple depths in a diffusing medium and in air were performed with the SIMSET simulation software package (37). Simulations take into

Received Jan. 27, 1997; revision accepted Jun. 12, 1997.

For correspondence or reprints contact: Philippe Maksud, Institut National de la Santé et de la Recherche Médicale Unité 66, Faculté de Médecine Pitié Salpêtrière, 91 Boulevard de l'Hôpital, 75634 Paris Cedex 13, France.

account Compton and photoelectric interactions. The following sources were considered:

1. -1 quasipunctual source: (sphere, radius = 0.1 cm) at 13 depths ranging from 1–29 cm;
2. -1 quasilinear source: (cylinder, radius = 0.1 cm, height = 15 cm) at 13 depths ranging from 1–29 cm;
3. -3 quasiplanar sources: sizes $0.1 \times 5 \times 5$ cm, $0.1 \times 10 \times 100$ cm and $0.1 \times 20 \times 200$ cm) at 9 depths ranging from 1–29 cm;
4. -1 spherical source: radius = 10 cm, with center at a depth of 15 cm;
5. -1 cylindrical source: radius = 10 cm, height = 15 cm with center at a depth of 15 cm.

Each simulation of 2 million detected photons took about 2 hr on a SUN SPARK 20 (Sun, Mountain View, CA). Parameters of the simulation were chosen to reproduce the characteristics of the system used in this study for real acquisitions (Helix camera; Elscint Ltd., Ra'anana, Israel) with HR-LE collimators (HPC-45). Images (64×64 pixels) of primary and scattered photons were obtained for 32 energy windows of 3.5 keV ranging from 70–182 keV.

Physical Phantoms: Radioactive Sources and Scintigraphic Acquisitions

Radioactive sources were placed in a large container ($20 \times 20 \times 200$ cm) either filled or not with water. Spheres (5, 15, 30, 65 and 100 cm (3) and a torus (100 cm (3) were filled with a solution of ^{99m}Tc . Activities in spherical sources ranged from 37 to 370 MBq (according to the size of the source) and was 37 MBq for the torus. Different source depths were used, ranging from 3 to 15 cm (step size: 2 cm). Scintigraphic acquisitions were realized with two diametrically opposed detectors and low-energy, high-resolution collimators (HPC-45). Acquisition time was chosen to detect about 1000 events in the hottest pixel. For each source, 32 images with an energy window of 3.5 keV, spanned between 70 and 182 keV were acquired. In addition, conventional images with a 20% energy window from 126–154 keV (F20) were acquired for comparison purposes.

Clinical Study

For the clinical study, anterior and posterior spectral images of the pelvis zone (32 energy windows, 70–182 keV, 150 s per image) were acquired 3 hr after the injection of 600 MBq to a 45-yr-old man referred to for a bone scintigram. To test the ability to correct for attenuation, half of the field (left part) was shadowed by a rectangular piece of Plexiglas (thickness = 1.5 cm) to get a 20% attenuation of signal in the posterior view.

Artificial Neural Network Architecture

The ANN used was a multilayer perceptron (MLP) featured with the error backpropagation algorithm as learning tool (39). This type of ANN has been found particularly convenient for the simulation of any numerical function. Implementation of this network was embedded in a software package developed in our laboratory and it runs on Macintosh computers (38).

An MLP is made of partly connected artificial neurons. Artificial neurons have some of the characteristics of the biological neuron. They generally have several inputs and one output. Inputs can be external data as well as outputs of other neurons. The effect of each input is regulated by a specific weight that carries part of the knowledge embedded in the MLP after the learning phase. A weighted sum of the inputs is used to calculate the activation of the neuron (its internal state) by the way of an activation function. Commonly used activation functions are nonlinear: sigmoid, logistic or hyperbolic tangent (40). This activation is propagated to the

next neurons via the output. The MLP are organized in multiple layers. The data are applied to a first layer referred to as input layer; the last layer, referred to as output layer yields the MLP results. These two layers are separated by the so called hidden layers. Each neuron of each layer has a connection with each neuron of the next layer.

The architecture of the MLP is entirely described by the number of neurons of each layer. For example, the notation ($18 \rightarrow H6 \rightarrow H4 \rightarrow O2$), describes an MLP composed of an input layer (eight neurons) two hidden layers (six and four neurons, respectively) and an output layer of two neurons.

Artificial Neural Network Learning

A learning phase with typical examples must precede the use of an MLP network for the analysis of new cases. The learning phase is supervised: each example given as input to the network is associated with a solution that is the expected network output. In our work, input data are derived from the anterior and posterior spectrum values for a given pixel whereas the expected output values are the pixel count in the scatter and attenuation free image (Fig. 1). Due to the overfitting problem (also called learning by heart: the network is often powerful enough to specifically recognize every example of the learning set) that can occur in this situation, the learning set is split into two parts: the first subset is referred to as the training set, the second one as the validation set. The training set is used for weights adjustment, the validation set is used for MLP efficiency evaluation and global convergence testing.

Here are the successive steps of a typical learning session:

All weights are initialized with random values. The network is then submitted to an iterative weight adjustment procedure:

1. An example from the training set is applied at the MLP input.
2. The output is calculated through activation propagation in the MLP.
3. The error between the network output and the expected output is computed.
4. The weights are adjusted through the error backpropagation algorithm that tends to minimize the error between the expected and calculated outputs.
5. Steps 1–4 are reiterated for the input data of the training set.
6. The root mean square error (RMS) and the ratio likelihood/maximum likelihood (RL), which are some of the criteria characterizing the quality of learning, are computed using the validation set of data. The selection of the best criterion must be in harmony with known characteristics of noise (see Discussion). RMS and RL expressions are detailed in the section Evaluation of Methods.

Steps 1–6 are repeated. Typically, the error reduces very quickly at the beginning of the learning phase, much slowly thereafter. On the training set, the error can be drastically reduced whereas a divergence may appear on the validation set when the network starts learning the samples of the training set by heart. The learning phase is halted when the divergence is detectable or when no significant reduction of the error is observed anymore. A set of weights (weight matrix) is obtained after each learning step. The set minimizing (or maximizing) one of the evaluation criteria (see below, evaluation paragraph) on the validation set is selected.

When learning is achieved, an evaluation phase is run using an independent set of data: the evaluation set.

Designing an ANN for Scattering and Attenuation Correction

General rules for designing an MLP architecture (number of hidden layers and number of neurons in each layer) are almost empirical (39). The design of the network has little influence on

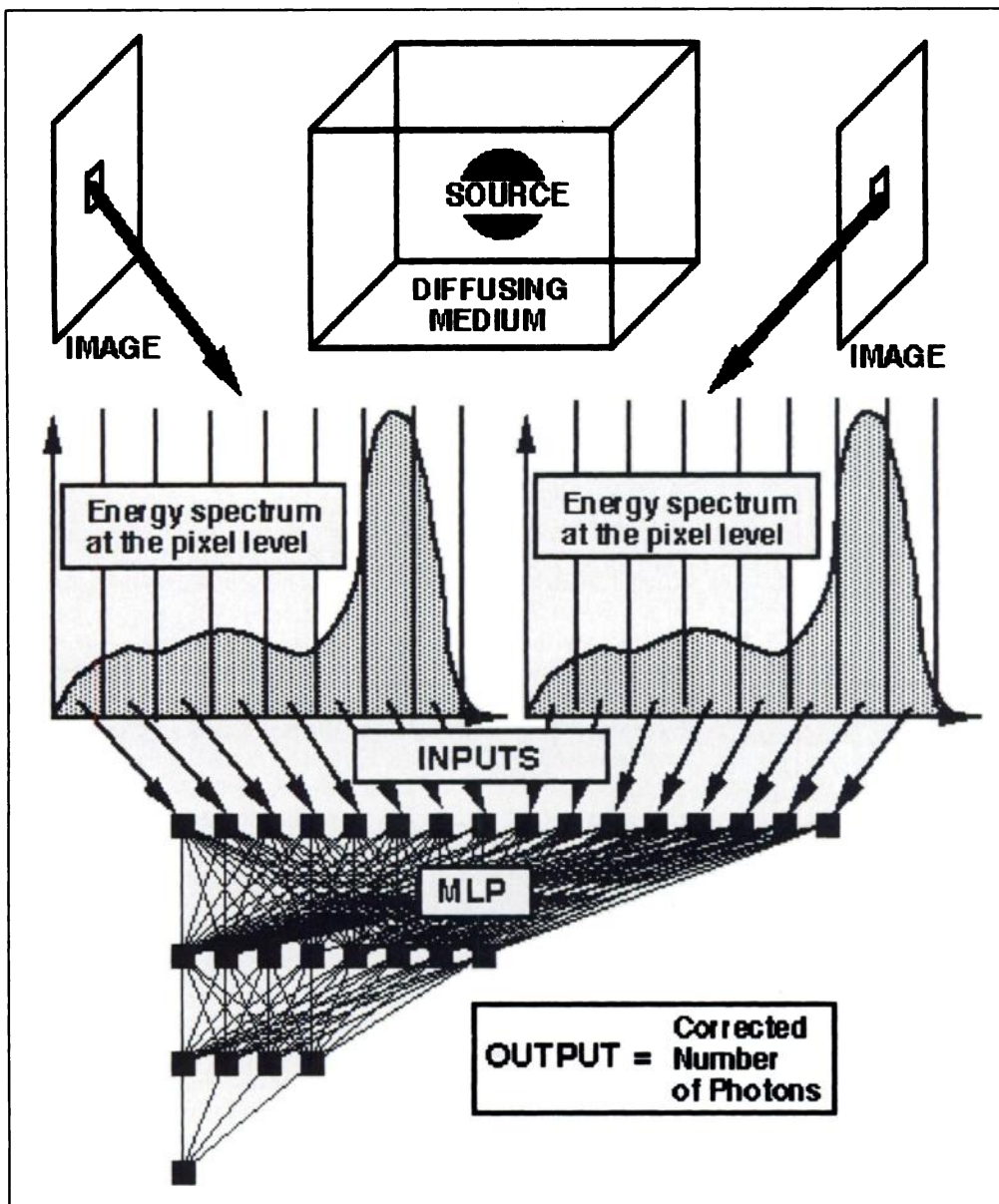


FIGURE 1. Design of the full system: each pixel provides a photon-energy spectrum which is given as part of the input to the network.

performance provided the number of neurons in the hidden layers exceeds a critical lower limit, and the training set is representative and large enough. As a rule of thumb, the number of hidden neurons being equal to half the sum of the input and output neurons is the critical lower limit. To meet these requirements, we have systematically used an MLP with two hidden layers and more neurons than strictly necessary in the hidden layers. Similarly, to avoid overfitting, the number of examples in the training set must be at least two to four times the number of weights. In these studies, the number of examples exceeded by more than 10 times the number of weights.

Pixel Selection for the Learning Phase

The MLP were trained on subsets of pixel data extracted from the learning images. Almost every image was symmetrical so that pixels in a quadrant or on lines drawn from the object center could be considered as representative of the whole image and, subsequently, were the only ones used.

Scattering Correction

Raw input data were composed of the energy spectrum observed in each pixel. These spectra were obtained either by simulation or by physical acquisition and sampled in 16 energy windows of 7 keV. The related output, yielded by a single neuron, was the ratio

of the primary photon count to the total detected photon count. Because we were only concerned with relative counts of photons, energy spectra given as inputs were normalized to the total count of photons. A two-hidden-layer MLP was used: (I16 → H8 → H4 → O1).

The training and validation sets were composed of pixels extracted from Monte Carlo-simulated images of the quasi linear radioactive source and of the three quasi planar radioactive sources at 6 depths (1–29 cm) in water (thickness 30 cm). 6210 pixels were retained for learning and 2430 for validation.

Composition of the Evaluation Set

Monte Carlo-simulated images of the quasi linear source at three depths (different from those used for MLP training) and of the spherical and cylindrical sources:

1. Physical acquisitions of the radioactive torus at 6 depths (5–15 cm) in water.
2. This set was designed to evaluate the MLP ability to generalize from the case of numerical simulations of linear and planar sources to that of numerical simulations of spherical and cylindrical sources and the case of real data (toric source). Making use of linear and planar source was

necessary to reproduce the great variety of spectra observed in reality for punctual to volumic sources.

Attenuation Correction

Under conditions of narrow-beam geometry, the transmission of a monoenergetic photobeam through an absorbing medium is described by an exponential equation:

$$I = I_0 \cdot \exp^{-\mu \cdot d/2},$$

where I is the beam intensity transmitted through a thickness d of absorber; I_0 is the intensity recorded in absence of absorber; and μ is the linear attenuation coefficient of the absorber at the photon energy of interest. In narrow-beam geometry, the calculation of the geometric mean (GM) of two opposite views (I_{ant} and I_{post}) of a punctual source in an attenuating medium can solve the problem of attenuation as far as the thickness (D) of the medium is known:

$$I = \text{GM} = \sqrt{I_{\text{ant}} \cdot I_{\text{post}}} = I_0 \cdot \exp^{-\mu \cdot D/2}.$$

With a distributed source a correction must be included to account for self-attenuation:

$$I = I_0 \cdot \left(\frac{\mu x/2}{\sinh(\mu x/2)} \right) \cdot \exp^{-\mu D/2},$$

where x is the thickness of source. However, in practice the thickness of source is usually not known so that the correction factor cannot be evaluated. We have subsequently used the GM in this work. In doing so, the resulting error for the intensity of the sources used in this work was almost negligible (see Discussion). An MLP was trained on numerical simulations of punctual sources with activities varying from 0 to 255 (arbitrary units), at various depths (five levels for each thickness), in a scattering and absorbing medium (five thicknesses, 10–30 cm).

The source activity was used as the target (expected output). Three sets of experiments were conducted:

1. Correction for attenuation was attempted on the mere basis of the counts in the conventional window from the anterior (I_{ant}) and posterior views (I_{post}) and the GM, given as inputs to MLP. A two-hidden-layer MLP was used: (I3 → H8 → H4 → O1).
2. The thickness of the scattering medium was given as additional input. A two-hidden-layer MLP was used: (I4 → H8 → H4 → O1).
3. The energy spectra (105–161 keV) from two opposite views distributed on 2×8 windows of 7 keV were used as inputs as an alternative to thickness. Spectra were obtained by Monte Carlo simulation of the punctual source at the same depths in water. A two-hidden-layer MLP was used: (I19 → H8 → H4 → O1).

Although not strictly necessary, the GM was added as input in every experiment because it was observed that it dramatically reduced the learning times. The comparison of calculated and simulated activities was done for the evaluation phase with 25 datasets obtained at different depths and thicknesses.

Simultaneous Scattering and Attenuation Correction

Images obtained from physical phantoms were used. The conventional window from anterior (I_{ant}) and posterior view (I_{post}), the GM ($\sqrt{I_{\text{ant}} \cdot I_{\text{post}}}$) and the energy spectra (105–161 keV) distributed on 2×8 windows of 7 keV (for each anterior and posterior view) were given as inputs. Counts in air were given as target. A two-hidden-layer MLP was used: (I19 → H16 → H8 → O1). MLP was trained, validated and evaluated on real acquisition data.

Data were extracted from a couple of opposite views of the real spherical radioactive sources (5, 30 and 100 cc) in air and water (30

cm thickness) with depths ranging from 3–15 cm (2 cm steps). Pixels 32130 were used for learning and 21726 for testing. The closest view obtained in air from the two opposite detectors was used as target.

Composition of Evaluation Sets

Evaluation sets were composed as follows:

1. Real acquisitions of the radioactive spherical source (65 cc), in water and air.
2. Real acquisitions of the radioactive torus (100 cc), in water and air.

Other Scatter Correction Methods

Compton Window Method (JZ). This method proposed by Jaszczak et al. (1) is based on an acquisition in a secondary Compton region window (from 92 to 125 keV). The scatter-corrected image is obtained by subtraction of the Compton window count, after normalization by a factor 0.5, from the photopeak window count.

Dual-Photopeak Window Method (KG). This method proposed by King et al. (3) uses two nonoverlapping energy windows (10%) located on each side of the photopeak. It hypothesizes the existence of a correlation between the scatter fraction (SF) and the ratio of the count in the lower window divided by the count in the upper window (R_S): $SF = A \cdot (R_S)^B + C$, where A , B and C are parameters to be estimated from dual-photopeak window acquisitions of a radioactive point source in an elliptical attenuator in air. The scatter-to-total ratio (STR) for each pixel is subsequently estimated by $STR = SF/(SF + 1)$. Typical values of 0.32, 1.9 and -0.15 , respectively, for A , B and C were obtained by King et al. but were found to give a systematic overcorrection for scattering in our work. These parameters have been subsequently estimated by fitting the dual photopeak model to the data corresponding to the linear source. Best A , B and C estimates were found to be 0.034, 4 and -0.1 .

Triple-Window Methods (OG1, OG2 and BG). These methods use three energy windows. The first one is the ordinary photopeak window and the two others are narrow-energy windows ($C1$ and $C2$) located on each side of the photopeak window. The scatter events (SE) in the photopeak window are estimated from the counts in windows $C1$ and $C2$ and the window sizes $W0$ (for the photopeak window), $W1$ and $W2$ (for the narrow-energy windows) by:

$$SE = (C1/W1 + C2/W2) \cdot W0/2 \quad (\text{OG1}) \text{ Ogawa et al. (5)}$$

$$\text{or } SE = C1/W1 \cdot W0/2 \quad (\text{OG2}) \text{ Ogawa et al. (6)}$$

$$\text{or } SE = (C1/W1 - C2/W2) \cdot W0/2 \quad (\text{BG}) \text{ Bourguignon et al. (41)}$$

Evaluation of Methods

Conventional images, images corrected by neural network or by other scatter correction methods, were compared to the reference images. For scattering correction, the reference images were primary photon images obtained by Monte Carlo simulations. For attenuation and scattering correction on physical phantoms, the image acquisitions obtained in air were considered as the reference. A visual evaluation of the correction was achieved by subtracting the corrected images from the reference image. Three criteria were used as global quantifiers of errors over the whole image:

Root mean square errors Recovery Likelihood:

$$\text{RMS} = \sqrt{\frac{1}{n} \sum_{i=1}^n (t_i - o_i)^2} \quad \text{RCV} = \frac{\sum_{i=1}^n o_i}{\sum_{i=1}^n t_i} \quad \text{LKD} = \prod_{i=1}^n \frac{(t_i) o_i}{o_i!} e^{-t_i},$$

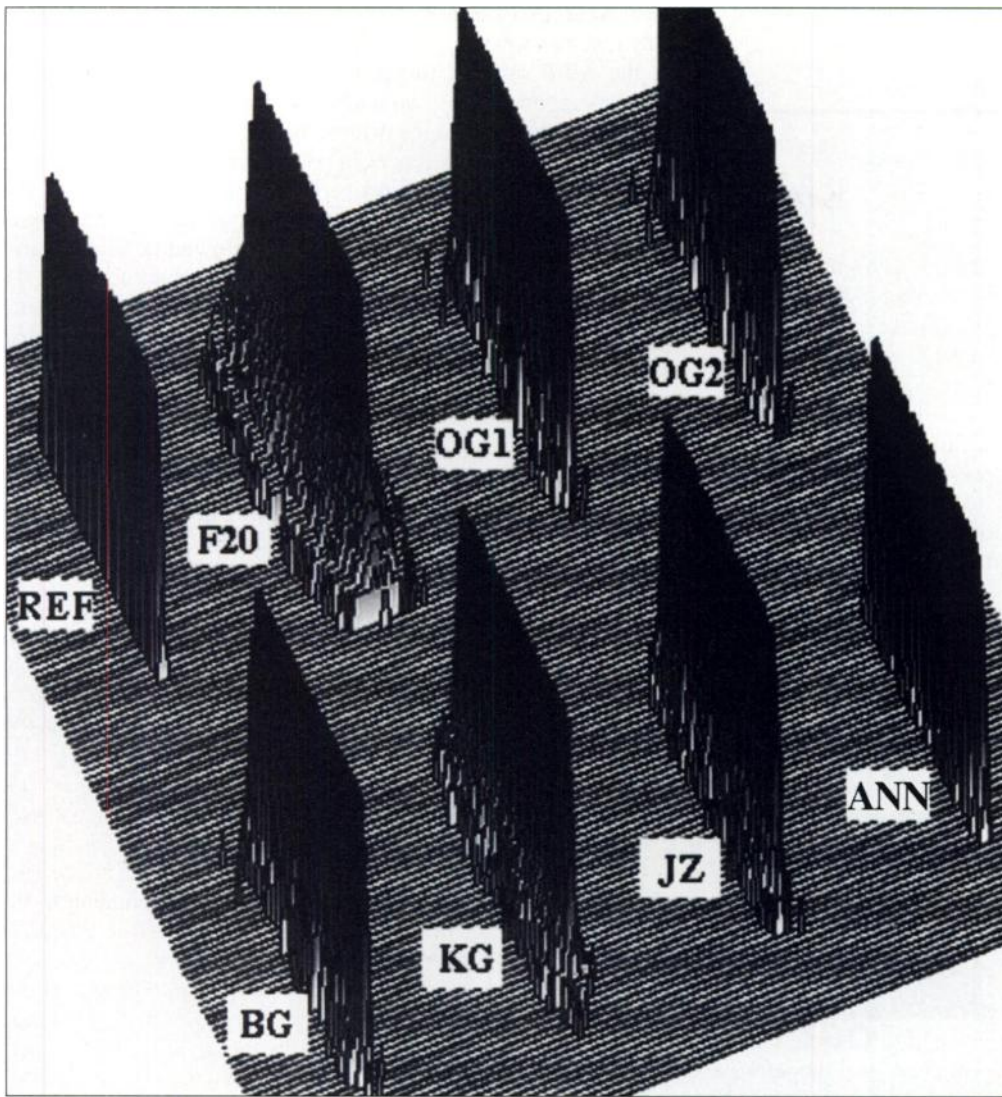


FIGURE 2. Examples of three-dimensional profiles obtained for scatter corrected images of the linear source at 12.5 cm depth. The three-dimensional profiles are labeled as follows: REF = profile for primary photons image; F20 = profile for conventional 20% window image. Corrected images are labeled according to the methods as follows: OG1 = first Ogawa method; OG2 = second Ogawa method; BG = Bourguignon method; KG = dual-photopeak method; JZ = Compton window method; ANN = neural network method. A logarithmic scale is used for the z-axis.

where t_i is the true pixel value, o_i is the value obtained by MLP and n the number of examples in the set.

For the likelihood, the results were expressed as RL: ratio of logarithm of likelihood to logarithm of maximum of likelihood (obtained for $t_i = o_i$).

RESULTS

Learning Time and Error Measurements

Depending on the size of the learning set, 5,000–10,000 cycles of data presentation were required to obtain a minimization of error estimates (20–40 hr of computing time). The evolution of the three-error criteria computed on the validation set were found nearly similar for all the learning phases. After a steep variation, the learning curves reached a plateau with no further improvement. Thanks to the important size and heterogeneity of the learning set ($n = 1,500\text{--}32,000$), no overfitting was observed during the learning phases. Therefore, the selection of the optimal weight matrix was not a decisive step: any matrix obtained in the learning plateau could be indifferently used.

Scattering Correction

The output expected from the MLP was the ratio of primary photon count to total photon count. Images were reconstructed from this ratio. The learning phase was exclusively conducted on data obtained from the linear and planar sources using Monte Carlo simulations.

Simulated Linear Source

Correction was almost perfect in the area of the source (Fig. 2), and the scattered part outside the source was strongly reduced. As a result, edges were sharper and contrast was enhanced. Corrections offered by other methods were less accurate, particularly in the edge regions and outside the source. As expected, performances of all methods degraded when source depth was increased (Table 1). However, the ANN

TABLE 1
Errors for Linear Source at 7.5, 12.5 and 25 cm

		F20%	OG1	OG2	BG	KG	JZ	ANN
RMS	7.5 cm	13.5	2.7	2.7	2.7	2.3	5.0	0.67
	12.5 cm	18.4	4.7	4.7	4.7	3.5	7.3	1.6
	25.0 cm	28.6	9.8	9.8	9.8	6.0	13.1	3.5
RCV (%)	7.5 cm	185	111	111	111	110	121	102
	12.5 cm	225	122	122	122	119	136	110
	25.0 cm	301	152	152	152	133	175	113
RL (%)	7.5 cm	0	68	68	68	87	31	96
	12.5 cm	0	17	17	17	28	3	79
	25.0 cm	0	2	2	2	21	0	45

RMS = root mean square error; RCV = recovery; RL = likelihood/maximum likelihood ratio; OG1, OG2 and BG = triple-window methods; KG = dual-photopeak window method; JZ = Compton window method; ANN = artificial neural networks.

TABLE 2
Errors for Spherical and Cylindrical Source

	F20%	OG1	OG2	BG	KG	JZ	ANN
Spheric source							
RMS	15.72	4.24	3.97	3.81	4.94	4.72	2.23
RCV (%)	162	95	96	98	112	97	101
RL (%)	1	24	27	30	37	27	67
Cylindrical source							
RMS	25.41	9.38	8.89	8.61	8.75	7.47	4.89
RCV (%)	158	92	94	96	108	95	98
RL (%)	0	8	10	12	22	21	48

See Table 1 for definitions.

consistently offered the best correction. It must be pointed out that, depending on the depth of sources, the different methods were more or less efficient (Table 1). For example, the JZ method appeared more fitted to small depths, whereas the three-window methods provided better results when depth is important.

Spherical and Cylindrical Simulated Sources

Quantitative evaluation performed on the whole image showed that the correction achieved by the MLP was still adequate, although slightly degraded, for spherical and cylin-

drical sources (Table 2). Others' methods behaved similarly, with results, however, consistently lower than those provided by the MLP. Visual inspection of source images and error images supported these conclusions (Fig. 3 for the cylindrical source). Corrected images offered by the MLP and JZ methods were the closest to reference. In particular, scattered photons in nonradioactive areas are properly discarded. A plot of the predicted count of photons, as a function of the expected count of photons (for the cylindrical source), allowed detailed examination of the corrections provided by the six methods (Fig. 4). Use of the 20% window resulted in photon counts that were systematically overestimated. In addition, the higher the photon count, the larger the error. This last phenomenon was clearly a consequence of the source geometry. No such bias was detectable when triple-window methods or the KG method were used, but corrections resulted in increased variability. The scatterplot for the JZ method indicated lower variability in the predictions, but hot spots were overcorrected. In contrast, MLP results were unbiased, while variability was kept small.

Toric Physical Phantom

Whatever the method, performances underwent further reduction (Table 3). The MLP method yielded the best results. In particular, the quality of correction did not rely on the depth of the source. A similar pattern is observed for the KG method, but

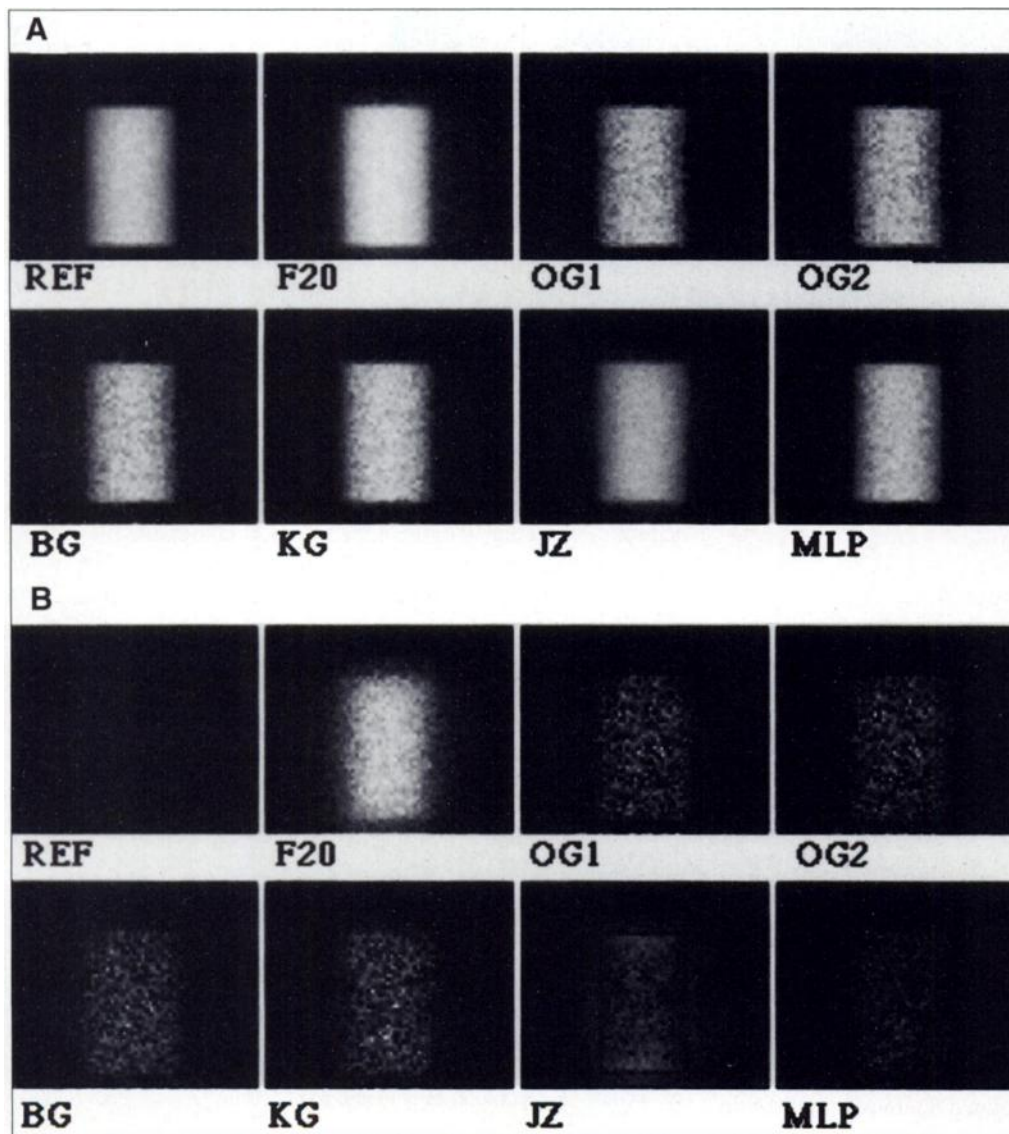


FIGURE 3. Scattering correction by six methods for the cylindrical source. Labels are similar to Figure 2. A logarithm scale is used to display the images. (A) Corrected images. (B) Error images obtained by subtraction of the primary photons image (target) from the scatter-uncorrected images (F20) and scatter-corrected images (as they appear in Fig. 3A).

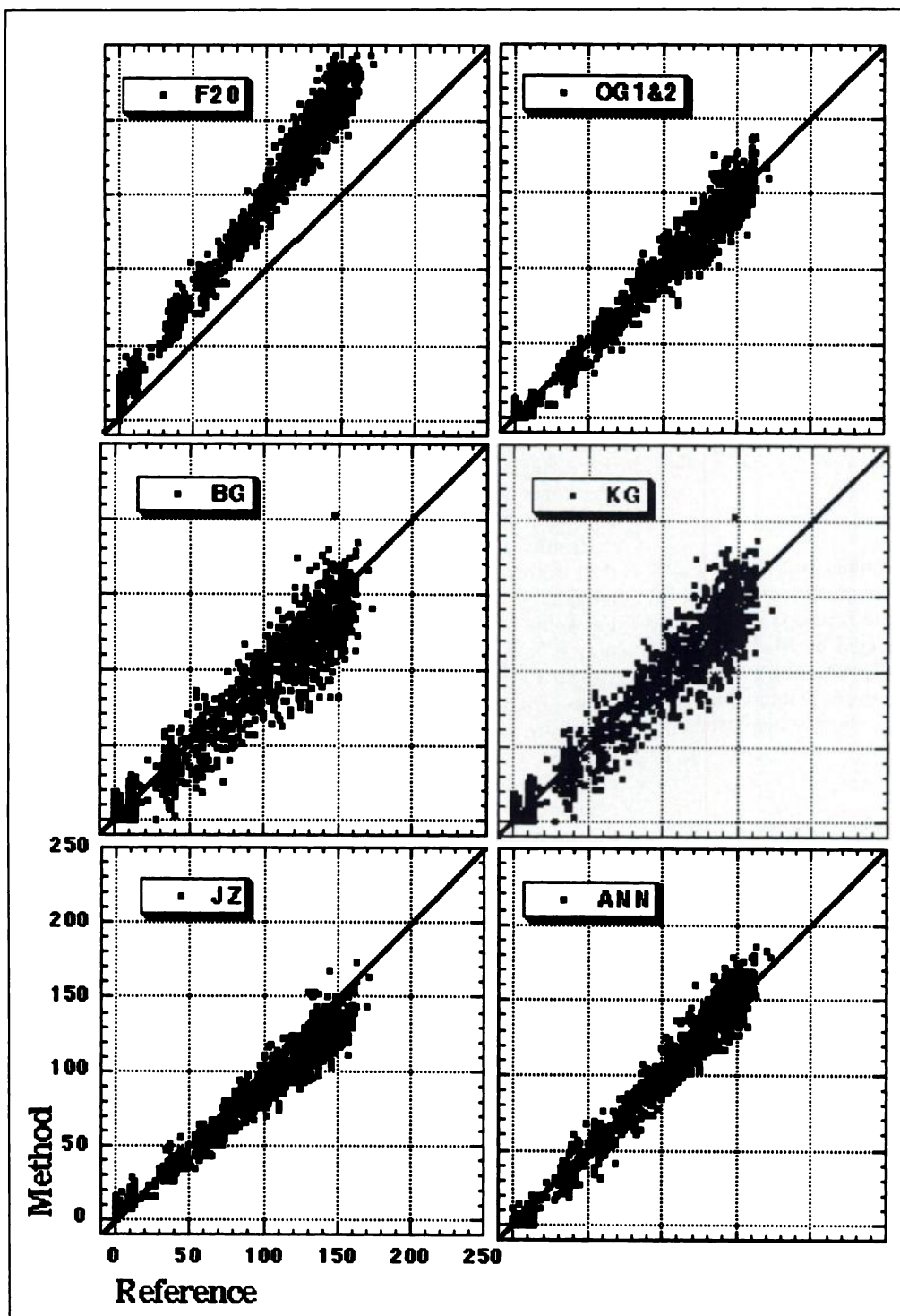


FIGURE 4. Graphs of pixel count corrected by the six scattering correction methods versus primary photons count. Labels are similar to Figure 2.

the level of correction is not as good. As has been previously observed with numerical simulations, the triple-window methods provided better results when depth is important.

Attenuation Correction

When the energy spectra (105–161 keV) from two opposite views were given, the MLP provided almost perfect attenuation correction regardless of the depth of the punctual source and the thickness of the attenuating medium (Fig. 5C). As expected, when the available data were only composed of the opposite counts in the 20% windows, the thickness of attenuating medium was required as input to the neural network to obtain an accurate correction (Fig. 5A and B).

Scattering and Attenuation Correction

For spherical sources as well as the torical source, the correction provided by MLP for scattering and attenuation was adequate (Table 4 and 5). The error was always lower than 10% regardless of depth. Noise was reduced and the edges were sharper than those obtained with the GM and even in air for regions without activity (Fig. 6A-C). Drastically better results than the GM method were obtained when depth was important [i.e., when diffusion played an important role (results not shown)]. For spherical sources, the mean density profile through the source almost exactly matches that obtained in air except on edges where a small but systematic overcorrection was detectable (Fig. 6D).

TABLE 3
Errors for Toric Source 100 cm³ at 5, 7, 11, 13 and 15 cm

		F20%	OG1	OG2	BG	KG	JZ	ANN
RMS	5 cm	14.3	11.4	10.3	9.44	9.42	7.86	8.5
	7 cm	12.5	13.9	12.8	11.8	7.22	6.98	6.58
	11 cm	15.9	14.4	13.3	12.3	7.60	8.33	6.26
	13 cm	21.0	7.98	7.38	6.10	9.56	11.3	7.42
	15 cm	22.4	8.8	7.97	7.39	8.68	11.7	6.60
RCV (%)	5 cm	122	91	92	94	105	105	103
	7 cm	122	88	89	91	103	104	98
	11 cm	131	90	91	93	105	105	99
	13 cm	146	100	102	103	116	123	110
	15 cm	147	99	100	102	115	123	109
RL (%)	5 cm	3	14	18	21	23	25	30
	7 cm	4	12	15	19	40	26	50
	11 cm	2	10	14	17	39	23	53
	13 cm	0	36	39	39	22	7	37
	15 cm	0	39	31	31	24	5	35

See Table 1 for definitions.

Corrections for pelvis scans were satisfactory (Fig. 7). The location of the piece of Plexiglas was clearly visible in the posterior view and was still perceptible in the GM image. In contrast, both sides of the image corrected by MLP displayed similar intensities as shown by the profile plot. The contrast was enhanced (e.g., hands and femurs were strongly intensified) and edges were sharper although noise was slightly increased.

DISCUSSION

Stopping Criterion for Learning Phase

The mean-square-error criterion is widely used to supervise the learning phase of MLP. This criterion is suited for Gaussian distribution of error. However, radioactive counts are distributed according to a Poisson law so that it could be advisable to maximize the likelihood (42). In practice, the evolution of these two criteria during the learning phases were almost similar in all cases. It is believed that these two criteria lead to similar conclusions probably because the most counts were higher than 30 in the datasets.

Scattering Correction

Qualitative and quantitative evaluation of scatter correction provided by our ANN show its ability to perform a scatter

TABLE 4
Errors for Real Sphere 65cc (Activity Range 0-255) at 13 cm Depth

	3 cm	5 cm	7 cm	9 cm	11 cm	13 cm
RMS	11.08	12.34	11.76	11.83	13.29	11.27
RCV (%)	94	98	109	109	96	95
RL (%)	38	26	24	23	23	33

See Table 1 for definitions.

correction from the energy spectrum observed in each pixel. The residual error (estimated by the square root of count in pixels) is at the level of the noise (Fig. 3B). Results obtained on the cylindrical and torical radioactive source show that the ANN can generalize to other shapes and work on real scintigraphic images, albeit with reduced efficiency. It is suggested that efficiency may be improved, using images of physical phantoms as learning data, provided a good scatter free reference is available.

Results obtained by MLP are at least equivalent to or better than the other methods used in this work. For greatest depths of radioactive sources, the difference in favor of MLP increases. For some of these methods (OG1, OG2, BG, KG), the correction is unbiased, but the variance is great compared to the variance observed for the image (F20% images, Fig. 4). This high variance may result from the small size of the energy windows used by these methods to correct for scattering. In contrast, a small variance is observed for the JZ method, but the correction is biased. An efficient posterior correction could be achieved by a fine tuning of the normalization factor. However, this ad hoc adaptation has to be made on a case-by-case basis.

Attenuation Correction

In narrow-beam conditions, a proper correction can be numerically achieved given the thickness of the attenuating medium and counts in two opposite views. We have shown that data dealing with thickness are embedded in the energy spectra in such a way that MLP can correct for attenuation without being explicitly given the thickness. However, practical problems of photon-beam attenuation in nuclear medicine usually happen under broad-beam conditions. Transmission of a source at depth *d* is increased by a factor *B* called the buildup factor (43). It is given by $T = \exp(-B\mu d)$, where *B* depends on the photon energy and on the source geometries. Therefore, we

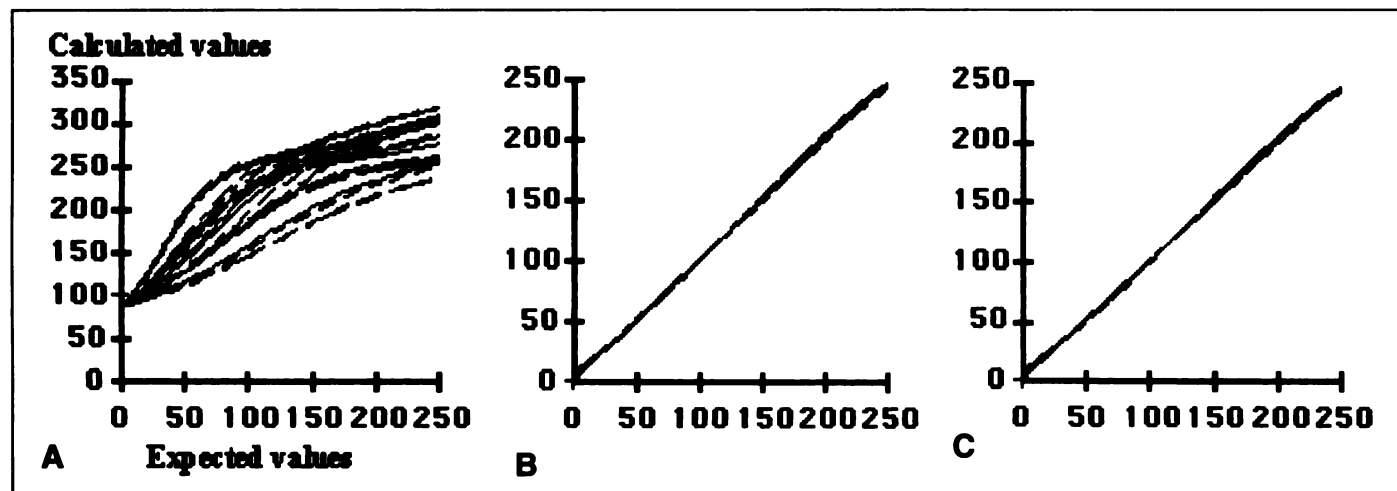


FIGURE 5. Comparison of activity values given by MLP and the real activity of a punctual source for the three sets of experiments when: (A) Iant, Ipost and GM are given to MLP, (B) Iant, Ipost, GM and thickness are given to MLP and (C) Iant, Ipost, GM and spectra are given to MLP (25 evaluation curves for each panel, each with different depths and thicknesses of attenuating medium).

TABLE 5
Errors for Toric Source 100 cm³ (Activity Range 0–255)
at 9 cm Depth

	3 cm	5 cm	7 cm	9 cm	11 cm	13 cm
RMS	15.97	15.78	14.22	13.47	12.63	11.77
RCV (%)	98	97	101	105	106	102
RL (%)	12	20	18	17	19	23

See Table 1 for definitions.

were not in a position to learn to correct for attenuation alone in broad-beam conditions so that we had to design a new network to simultaneously handle attenuation and scattering. Considering that thickness information is usually not available in clinical situations, especially for static or dynamic imaging, both spectra have been considered thereafter with the goal of both attenuation and scattering correction.

Scattering and Attenuation Correction

Proper correction of scatter and attenuation is provided by MLP when physical phantoms are used. However, the target used for the learning phase is an image obtained in air. The scattering and attenuation by air is negligible, but a problem arises from the scattering and attenuation involved by the source itself. The learning set includes small-sized sources for which scattering and self-attenuation are low. Self-attenuation in the source ranges from 0.2% (1-cc source) to 4% (100-cc source) and was not considered. Figure 6 shows that the result obtained by MLP processing on a sphere placed in a diffusing

medium exhibits lower counts outside the object than for the same sphere placed in air. The systematic overcorrection made by the neural network outside the biggest sources can be understood as a valid correction made to the reference images. Besides, corrections were made without considering the neighborhood of pixels. As a matter of fact, values of close pixels are correlated, and they could be used to improve the accuracy of the correction method. The correction offered for the images of the pelvis is subjectively clinically useful, especially if we consider that the network used for this task has been trained with images obtained in conditions quite different from those prevailing in the initial clinical study (heterogeneous diffusing medium and variable thickness). In particular, the vanishment of the effect on the piece of Plexiglas suggests that attenuation correction is realistic.

Noise

The ability to work on data spoiled by noise is a fundamental property of ANN (44). Neural networks are generally robust with noisy data (even chaotic in the mathematical sense), whereas such situations are devastating to most other techniques. This property has been implicitly called for during the learning phase of our ANN by using noisy simulations or acquisitions. The noise level of the learning data were similar to that of real acquisitions, and the size of these learning datasets were chosen so that multiple samples of similar but noisy spectra were available. We may wonder whether the process of spectra normalization eliminates the absolute count/noise magnitude information. In fact, after normalization to total photon counts, spectra obtained with a small number of photons are

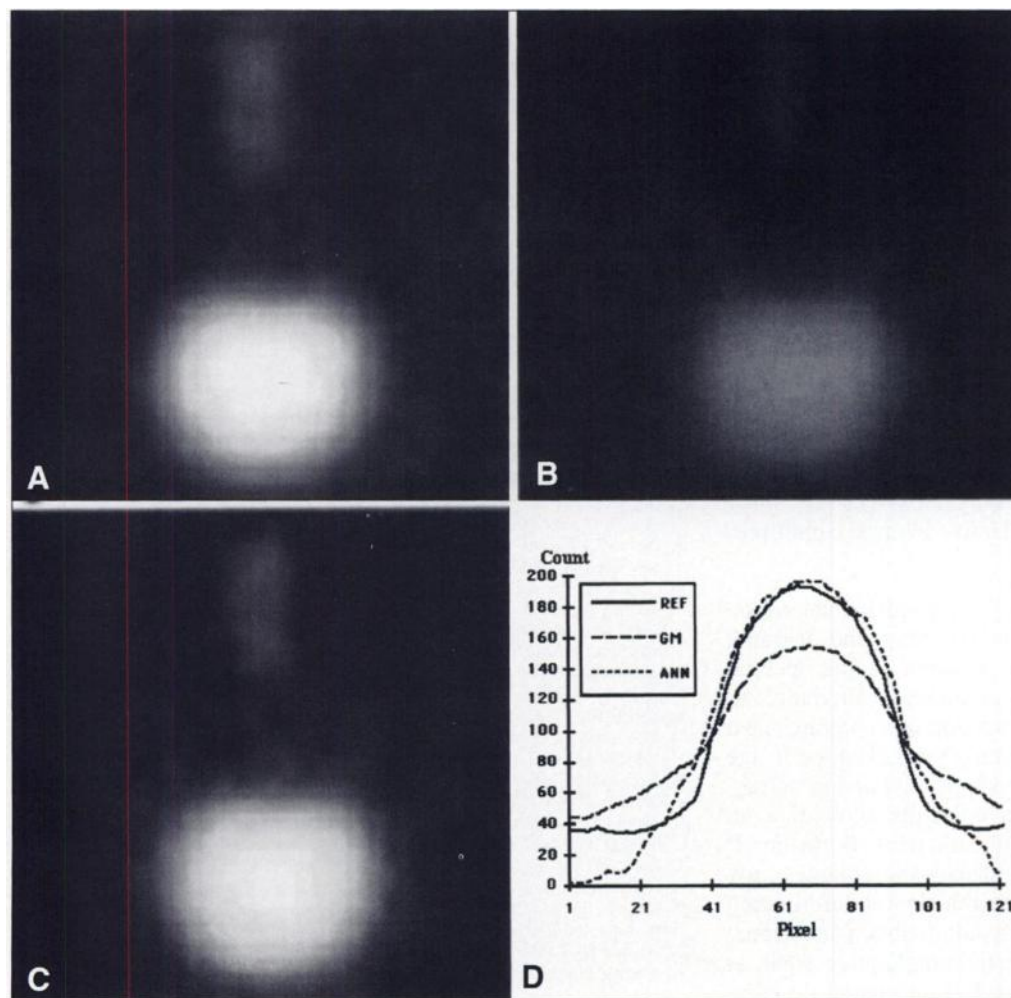


FIGURE 6. Results for the spherical source 65 cc: (A) image in air, (B) image obtained using the GM, (C) image corrected by neural network. (D) Count profiles along a diameter: REF labels the profile in air; GM labels the profile obtained using the GM; and ANN labels the profile obtained from the image corrected by neural network. A logarithm scale is used to display the images.

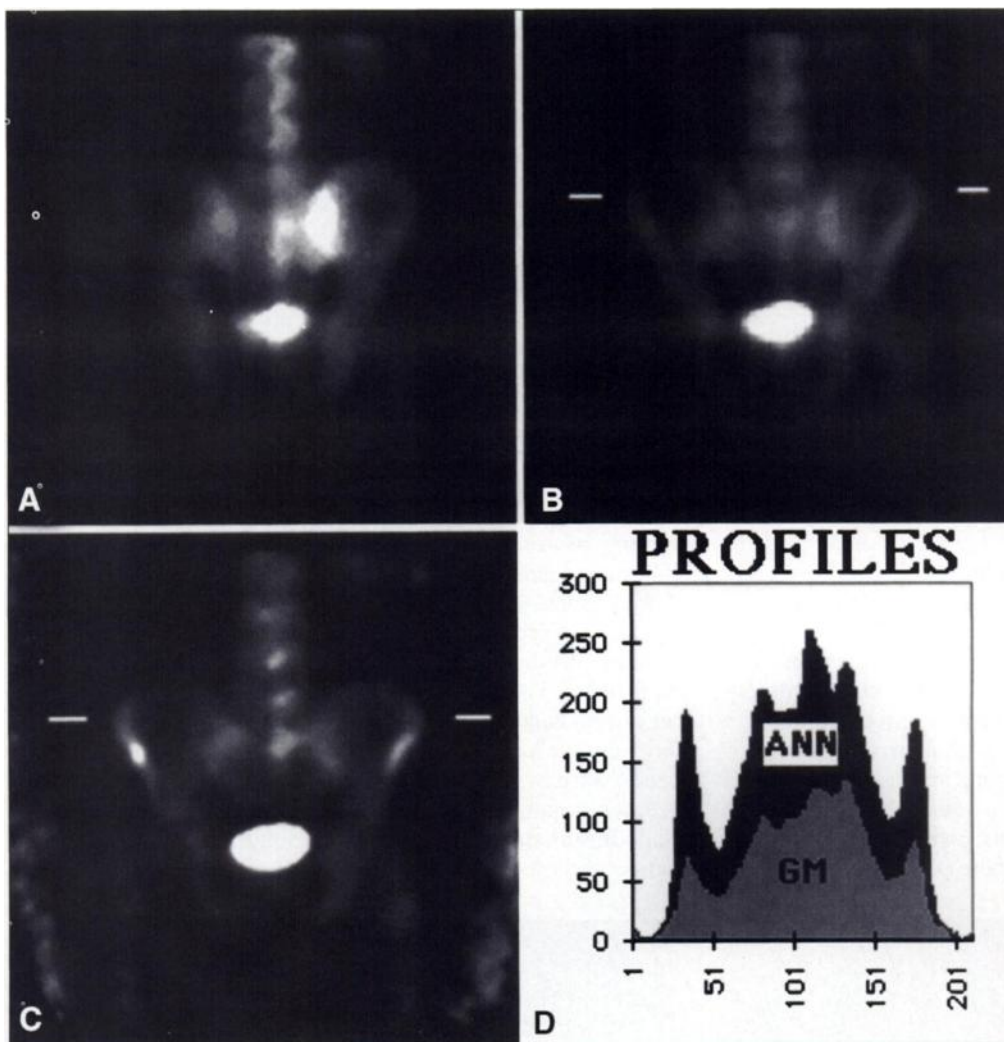


FIGURE 7. Simultaneous correction for scatter and attenuation in a human pelvis scintigraphy: (A) posterior view impaired by a rectangular piece of Plexiglas, (B) GM of posterior and anterior view, (C) image corrected by the network, (D) intensity profiles along a line through images B and C (location shown by marks).

highly variable (among consecutive channels within each spectrum), in contrast to those obtained with a high number of photons. Variability of counts among channels in a given spectrum as observed after normalization still provides MLP with some information dealing with absolute count/noise ratios. As described previously by Munley et al. (36), a slight increase of noise after correction by MLP is still detectable, especially in the low-count area in the pelvic clinical study. In our experiments, the counts in energy windows are often low, which results in high variability and reduces the accuracy of the results. However, contrast-enhancement, which is observed for hands and femurs (lying in low-activity areas) in this study indicates that the correction is still effective in these conditions.

CONCLUSION

Thanks to its comparative facility of implementation on various computers, robustness, rapidity (after the learning phase!) and success in the analysis of scintigraphic spectral images, the ANN approach provides an attractive alternative to classical techniques. The neural network approach requires no a priori knowledge about the distribution of radioisotope in the source (in contrast to the other methods of attenuation correction). Both qualitative and quantitative results show that an excellent correction can be made by a neural network method if the homogeneous sources of various shapes and volumes sank in a homogeneous medium with uniform thickness. Information from two opposite spectra seems sufficient to obtain an adapted correction in this context. Additional complexities such as heterogeneity in absorbing medium and in the spatial distribu-

tion of radioactivity necessitate further investigations to specify fields of possible applications and to better surround the validity of this method.

REFERENCES

1. Jaszczak RJ, Greer KL, Floyd CE, Harris CC, Coleman R. Improved SPECT quantitation using compensation for scattered photons. *J Nucl Med* 1984;25:893-900.
2. La Fontaine R, Stein MA, Graham LS, Winter J. Cold lesions: enhanced contrast using asymmetric photopeak windows. *Radiology* 1986;160:255-260.
3. King MA, Hademos GJ, Glick SJ. A dual-photopeak windows methods for scatter correction. *J Nucl Med* 1992;33:605-612.
4. Ichihara T, Ogawa K, Motomura N, Kubo A, Hashimoto S. Compton scatter compensation using the triple-energy window method for single- and dual-isotope SPECT. *J Nucl Med* 1993;34:2216-21.
5. Ogawa K, Harrata Y, Ichihara T, Kubo A, Hashimoto S. A new method for scatter correction in SPECT. *J Nucl Med* 1990;17:518.
6. Ogawa K, Harrata Y, Ichihara T, Kubo A, Hashimoto S. A practical method for position-dependent Compton-scatter correction in single-photon emission CT. *IEEE Trans Med Imag* 1991;10:408-412.
7. Yanch JC, Flower MA, Webb S. Improved quantification of radionuclide uptake using deconvolution and windowed subtraction techniques for scatter compensation in single-photon emission computed tomography. *Med Phys* 1990;17:1011-1022.
8. Yanch JC, Flower MA, Webb S. A comparison of deconvolution and windowed subtraction techniques for scatter compensation in SPECT. *IEEE Trans Med Imag* 1988;7:13-20.
9. Axelsson B, Msaki P, Israelsson A. Subtraction of Compton-scattered photons in SPECT. *J Nucl Med* 1984;25:490-494.
10. Floyd CE, Jaszczak RN, Greer KL, Coleman RE. Deconvolution of Compton scatter in SPECT. *J Nucl Med* 1985;26:403-408.
11. Koral KF, Wang X, Rodgers WL, Clinthorne NH. SPECT Compton scattering correction by analysis of energy spectra. *J Nucl Med* 1988;29:195-202.
12. Maor D, Berlad G, Chrem Y, Soil A, Todd Pokropek AE. Klein Nishina-based factors for Compton-free imaging. *J Nucl Med* 1991;29:195-202.
13. Gagnon D, Todd-Pokropek A, Arsenault A, Dupras G. Introduction to holospectral imaging in nuclear medicine for scatter subtraction. *IEEE Trans Med Imag* 1989;8:245-250.

14. Gagnon D, Pouliot N, Laperrière L. Statistical and physical content of low-energy photons in holospectral imaging. *IEEE Trans Med Imaging* 1991;10:284-289.
15. Morvan D, Bazin JP, Cavailloles F, Di Paola R. Correction of scattering effects by factor analysis: a simulation of a clinical study. Proceedings of the 25th Congress of the SNME. Stuttgart: Schattauer Verlag; 1988:41-44.
16. Mas J, Ben Younes R, Bidet R. Improvement of quantification in SPECT studies by scatter and attenuation compensation. *Eur J Nucl Med* 1989;15:351-356.
17. Mas J, Hannequin P, Ben Younes R, Bellaton B, Bidet R. Scatter correction in planar imaging and SPECT by constrained factor analysis of dynamic structures (FADS). *Phys Med Biol* 1990;35:1451-1465.
18. Buvat I, Frouin F, Ricard M, Bazin JP, Aubert B, Di Paola R. Compton-scatter correction by constrained factor analysis of spectral structures (CFASS) [Abstract]. *Eur J Nucl Med* 1990;16:403.
19. Buvat I, Benali H, Frouin F, Bazin JP, Di Paola R. Target apex-seeking in factor analysis of medical image sequences. *Phys Med Biol* 1993;38:123-138.
20. Zhou YT, Chellapa R, Vaid A, Jenkins BK. Image restoration using a neural network. *IEEE Trans Acoust Speech Signal Processing* 1988;36:1141-1151.
21. Qian W, Kallergi M, Clarke LP. Order statistic-neural network hybrid filters for camera-bremsstrahlung image restoration. *IEEE Trans Med Imag* 1993;12:58-64.
22. Floyd CE, Tourassi GD. An artificial neural network for lesion detection on single-photon emission computed tomographic images. *Invest Radiol* 1992;27:667-72.
23. Lo SC, Freedman MT, Lin JS, Mun SK. Automatic lung nodule detection using profile matching and back-propagation neural network techniques. *J Digit Imaging* 1993;6:48-54.
24. Cavouras D, Prassopoulos P. Computer image analysis of brain CT images for discriminating hypodense cerebral lesions in children. *Med Inf (London)* 1994;19:13-20.
25. Dorffner G, Porenta G. On using feedforward neural networks for clinical diagnostic tasks. *Artif Intell Med* 1994;6:417-35.
26. Floyd CE, Lo JY, Yun AJ, Sullivan DC, Kornguth PJ. Prediction of breast cancer malignancy using an artificial neural network. *Cancer* 1994;74:2944-2948.
27. Fujita H, Katafuchi T, Uehara T, Nishimura T. Application of artificial neural network to computer-aided diagnosis of coronary artery disease in myocardial SPECT bull's-eye images. *J Nucl Med* 1992;33:272-276.
28. Kippenhan JS, Barker WW, Pascal S, Nagel J, Duara R. Evaluation of a neural-network classifier for PET scans of normal and Alzheimer's disease subjects. *J Nucl Med* 1992;33:1459-67.
29. Kippenhan JS, Barker WW, Nagel J, Grady C, Duara R. Neural-network classification of normal and Alzheimer's disease subjects using high-resolution and low-resolution PET cameras. *J Nucl Med* 1994;35:7-15.
30. Porenta G, Dorffner G, Kundrat S, Petta P, Duit SJ, Sochor H. Automated interpretation of planar thallium-201-dipyridamole stress: redistribution scintigrams using artificial neural networks. *J Nucl Med* 1994;35:2041-2047.
31. Scott JA, Palmer EL. Neural network analysis of ventilation-perfusion lung scans. *Radiology* 1993;186:661-664.
32. Tombropoulos R, Shiffman S, Davidson C. A decision aid for diagnosis of liver lesions on MRI. *Proc Annu Symp Comput Appl Med Care* 1993;32:439-443.
33. Tourassi GD, Floyd CE, Sostman HD, Coleman RE. Acute pulmonary embolism: artificial neural network approach for diagnosis. *Radiology* 1993;189:555-558.
34. Erler BS, Hsu L, Truong HM, et al. Image analysis and diagnostic classification of hepatocellular carcinoma using neural networks and multivariate discriminant functions. *Lab Invest* 1994;71:446-451.
35. Ogawa K, Nishizaki N. Accurate scatter compensation using neural networks in radionuclide imaging. *IEEE Trans Nucl Sci* 1993;40:1020-1025.
36. Munley MT, Floyd CE Jr, Bowsler JE, Coleman RE. An artificial neural network approach to quantitative single-photon emission computed tomographic reconstruction with collimator, attenuation and scatter compensation. *Med Phys* 1994;21:1889-1899.
37. Harrison RL, Vannoy SD, Gillipsie SB, Kaplan MS, Luellen TK. Preliminary experience with the photon history generator module of a public domain simulation system for emission tomography. *Conference Record of the 1993 IEEE Nuclear Science Symposium and Medical Imaging Conference* 1994;2:1154-1158.
38. Aurengo A, Hejblum G, Maksud P, Rica C. Nominative object-oriented programming. Application to interactive image analysis including symbolic processing. *MEDINFO 92*. 1992;2:446-451.
39. Rumelhart DE, Hinton GE, Williams RJ. Learning internal representation by error propagation. In: Pres M, ed. *Parallel distributed processing*. Cambridge MA: MIT Press; 1986:318-362.
40. Masters T. *Practical neural networks recipes in C++*. A.P. Limited ed. San Diego CA; 1993.
41. Bourguignon M, Wartski MN, Berrah H, et al. Le spectre du rayonnement diffusé dans la fenêtre du photopic: analyse et proposition d'une méthode correction. *Med Nucl* 1993;17:53-58.
42. Muller SP, Kijewski MF, Moore SC, Holman BL. Maximum-likelihood estimation: a mathematical model for quantitation in nuclear medicine. *Med Phys* 1990;10:1693-1701.
43. Wu RK, Siegel JA. Absolute quantitation of radioactivity using the buildup factor. *J Nucl Med* 1984;11:189-192.
44. Hornik K. Approximation capabilities of multilayer feedforward networks. *Neural Networks* 1984;4:251-257.

Supercomputer Description of Human Lung Morphology for Imaging Analysis

T.B. Martonen, D. Hwang, X. Guan and J.S. Fleming

Experimental Toxicology Division, U.S. EPA, Research Triangle Park, and Division of Pulmonary Diseases, Department of Medicine, University of North Carolina, Chapel Hill; Microelectronics Division, IBM Corporation, Research Triangle Park; Center for Extrapolation Modeling, Department of Medicine, Duke University, Durham, North Carolina; and Department of Nuclear Medicine, Southampton General Hospital, Southampton, United Kingdom

A supercomputer code that describes the three-dimensional branching structure of the human lung has been developed. The algorithm was written for the Cray C94. In our simulations, the human lung was divided into a matrix containing discrete volumes (voxels) so as to be compatible with analyses of SPECT images. The matrix has 3840 voxels. The matrix can be segmented into transverse, sagittal and coronal layers analogous to human subject examinations. The compositions of individual voxels were identified by the type and respective number of airways present. The code provides a mapping of the spatial positions of the almost 17 million airways in human lungs and unambiguously assigns each airway to a voxel. Thus, the clinician and research scientist in the medical arena have a powerful new tool to be used in imaging analyses. The code was designed to be integrated into diverse applications,

including the interpretation of SPECT images, the design of inhalation exposure experiments and the targeted delivery of inhaled pharmacologic drugs.

Key Words: computer simulation; lung morphology; voxel structure; imaging analysis; aerosol therapy

J Nucl Med 1998; 39:745-750

Knowledge regarding the spatial distribution patterns of inhaled particles has critical implications for medicine and toxicology, in basic research and practice. For instance, aerosol therapy protocols would be enhanced if pharmacologic drugs could be selectively deposited at appropriate sites (e.g., receptors) within human lungs to elicit optimum therapeutic effects. In addition, risk assessment regimens for air pollutants would be improved if the localized doses delivered to sensitive airway cells could be quantitated.

With the advancement of planar gamma camera and SPECT technologies, the resolution of laboratory imaging processes has steadily increased. For example, when using a two-head SPECT instrument the three-dimensional distribution of an inhaled aerosol deposition pattern can be measured. If aligned anatomical imaging such as CT or MRI is also performed, then the deposition pattern may be related to the anatomical outline of

Received Jun. 9, 1997; accepted Aug. 13, 1997.

For correspondence or reprints contact: T.B. Martonen, PhD, Mail Drop 74, Experimental Toxicology Division, U.S. EPA, Research Triangle Park, NC 27711.

This manuscript has been reviewed in accordance with the policy of the National Health and Environmental Effects Research Laboratory, U.S. Environmental Protection Agency, and approved for publication. Approval does not signify that the contents necessarily reflect the views and policies of the agency, nor does mention of trade names or commercial products constitute endorsement or recommendation for use.

Editor's Note: This manuscript was submitted with 14 additional figures and 12 additional tables. This data was viewed as important material but represented inefficient use of journal space. This material can be obtained by accessing the SNM home page via the Internet: <http://www.snm.org>.